IEEE Access
Multidisciplinary | Rapid Review | Open Access Journal

Received July 4, 2019, accepted August 9, 2019, date of publication August 28, 2019, date of current version September 24, 2019.

Digital Object Identifier 10.1109/ACCESS.2019.2937966

Nonlocal Means Image Denoising With Minimum MSE-Based Decay Parameter Adaptation

YI ZHAN[1], JINBO WU[2], MINGYUE DING[1], AND XUMING ZHANG[1]

[1]Key Laboratory of Molecular Biophysics, School of Life Science and Technology, Ministry of Education, Huazhong University of Science and Technology, Wuhan 430074, China
[2]School of Naval Architecture and Ocean Engineering, Huazhong University of Science and Technology, Wuhan 430074, China

Corresponding author: Xuming Zhang (zxmboshi@hust.edu.cn)

This work was supported in part by the National Key Research and Development Program of China under Grant 2017YFB1303100, and in part by the National Natural Science Foundation of China under Grant 61871440.

ABSTRACT Nonlocal means (NLM), a patch-based nonlocal recovery paradigm, has attracted much attention in recent decades. The decay parameter will greatly affect restoration performance of the NLM method. However, the existing NLM methods with decay parameter adaptation cannot determine this parameter effectively. To address this problem, we have proposed the minimum mean square error (MSE) based decay parameter adaptation method for the NLM denoising. In the proposed method, the globally optimal decay parameter is determined to produce the pre-denoised image based on the derived relation between the global minimum MSE and the decay parameter. Then, the pixel-wise MSE is estimated based on the pre-denoised result and the corresponding method noise. Finally, the optimal pixel-wise decay parameter is obtained by minimizing the pixel-wise MSE to produce the estimated restored image and the boosting strategy is implemented on this image to generate the final denoised result. Extensive simulations on the standard test images and real images corrupted with Gaussian noise and speckle noise demonstrate that the proposed method significantly outperforms some compared NLM methods in noise reduction and detail preservation and can provide better restoration performance than other state-of-the-art denoising methods in most cases in terms of objective metrics and human vision.

INDEX TERMS Nonlocal means, decay parameter, mean square error, Gaussian noise, speckle noise.

I. INTRODUCTION

Noise will affect image quality, and lead to difficulty in pattern recognition. Therefore, denoising is a crucial step to facilitate subsequent image processing such as segmentation, registration and visualization. For several decades, various denoising techniques have been presented for noise removal such as wavelet based methods [1], partial differential equations (PDE) based methods [2], total variation based methods [3], [4], nonlocal means (NLM) methods [5] and deep learning based methods [6]. Among these methods, the NLM method has attracted much attention in the field of image denoising. This method was originally designed for Gaussian noise reduction, and it has been extended to suppress speckle noise inherent in ultrasound (US) imaging and synthetic aperture radar (SAR) imaging.

The traditional NLM method explores image self-similarities for noise removal by replacing the local comparison of individual pixels with the nonlocal comparison of image patches. In this method, the restored intensity $u(x, y)$ of the pixel at (x, y) in the noisy image I is presented as:

$$u(x,y) = \mathbb{NL}[I](x,y) = \frac{\sum\limits_{(p,q)\in\Omega} I(p,q)\omega(x,y,p,q)}{\sum\limits_{(p,q)\in\Omega} \omega(x,y,p,q)}, \quad (1)$$

where $\mathbb{NL}$ denotes the nonlocal means, and Ω is a search window. The weight $\omega(x, y, p, q)$ denoting the similarity between two pixels at (p, q) and (x, y) is calculated as:

$$\omega(x,y,p,q) = \exp\left(-\frac{||I(P(p,q)) - I(P(x,y))||^2_{2,a}}{h^2}\right), \quad (2)$$

where h denotes the decay parameter controlling the filtering degree, $P(p, q)$ and $P(x, y)$ are the two similarity windows (image patches) centered at (x, y) and (p, q), respectively; $||I(P(p, q)) - I(P(x, y))||^2_{2,a}$ means the weighted Euclidean distance between two image patches $P(p, q)$ and $P(x, y)$ of

The associate editor coordinating the review of this article and approving it for publication was Peng Liu.

size $(2L_p+1)\times(2L_p+1)$ defined as:

$$||I(P(p,q))-I(P(x,y))||^2_{2,a}=\sum_{i=-L_p}^{L_p}\sum_{j=-L_p}^{L_p}G_a(i,j)(I(p+i,q+j)-I(x+i,y+j))^2, \quad (3)$$

where $G_a(i,j)=\frac{1}{\sqrt{2\pi}a}\exp(-\frac{i^2+j^2}{2a^2})$ is the Gaussian kernel with the standard deviation $a>0$.

The restoration performance of the NLM method is greatly influenced by such parameters as the decay parameter, the search window and similarity window sizes as well as the weight computation strategy. To ensure good restoration performance in the case of Gaussian noise, the variations of this method have been proposed such as the search window adaptation [7]–[9], the similarity window adaptation [10], the iterative [11] or collaborative filtering schemes (e.g. BM3D [12]) as well as the improved weight computation based on principal component analysis (PCA) [13] and orthogonal moments [14]. For the NLM denoising of speckle-noise corrupted images, the related strategies include the similarity calculation methods based on the weighted maximum likelihood estimation framework [15], [16], Bayesian framework [17], [18], multiscale strategy [19], [20], maximum a posteriori [21], PCA [22] and test statistics [23], [24] as well as the combination of the NLM method with the sigma filter [25], the Kalman filter [26], the Lee filter [27], the Kuan filter [28], the guided filter [29], the total variation [30] and the wavelet shrinkage [31].

Despite the performance improvement of the above NLM methods over the traditional one, the optimal choice of the decay parameter still maintains an open and challenging problem. Recently, some decay parameter adaptation methods have been proposed. The global adaptation methods were proposed in [5], [8], [32] to determine a linear relation between the decay parameter h and the noise standard deviation σ for the whole image, i.e., $h=C\sigma$, where C denotes a constant. However, some researches in [13], [33] confirmed that the optimal h is only roughly proportional to σ in terms of peak signal-to-noise ratio (PSNR). Ville and Kocher [34] exploited a Stein's unbiased risk estimate (SURE) method to monitor the mean square error of the NLM method to determine the globally optimal decay parameter.

Although the above global decay parameter adaptation methods can enhance the robustness of the NLM method, a globally optimal h still makes it difficult to denoise the entire image without blurring any area in this image too much [35]. Therefore, the local adaptation of the decay parameter is an urgent need for NLM image denoising. Along this line, Duval *et al.* [35] introduced the bias-variance trade-off principle into the NLM method to highlight the need of the local choice of h and adaptively set h relying on the pixel-wise SURE (PSURE) method. Considering that the pixel-wise estimation of the risk is not robust, Duval et al. locally averaged the estimations based on the assumption that the risk is roughly homogeneous within each image region. This method tends to lead to the degraded restoration performance in some edge regions. Doré and Cheriet [36] deduced that the decay parameter corresponds to the bandwidth of a local constant regression and optimized h for each pixel by embedding a C_p statistic method into the Newton's method. However, this C_p-NLM method estimated the local MSE based on the noisy image, thereby leading to the inaccurate estimation of h at high noise levels.

On the whole, the existing NLM methods with decay parameter adaptation cannot determine this parameter for each image pixel accurately, thereby influencing their restoration performance for Gaussian-noise and speckle-noise corrupted images, especially at high noise contamination. To address this problem, we have proposed the minimum mean square error (MSE) based decay parameter adaptation framework for the NLM method. In the proposed method, the global minimum MSE derived from the Gaussian noise and speckle noise models is utilized to generate the pre-denoised image. The obtained denoised result and the corresponding method noise are utilized to estimate the pixel-wise MSE. The optimal decay parameter for each image pixel is estimated by minimizing the pixel-wise MSE using the steepest descent method to obtain the estimated restored image, based on which the boosting strategy is implemented to generate the final denoised image. Extensive simulations on several standard test images show that the proposed method outperforms several compared NLM methods in each case and the BM3D in most cases by providing higher PSNR and structural similarity (SSIM), and performs better than the compared deep learning based method [6] in some cases in terms of SSIM. Besides, testing on the real images demonstrates the advantage of the proposed method over other NLM methods in terms of SNR and contrast-to-noise ratio (CNR).

The reminder of this paper is organized as follows. Section II provides a detailed description of our method. Section III provides the experimental results and comparisons of restoration performance among the proposed method and other evaluated methods. Conclusions are drawn in Section IV.

II. METHOD

A. DEFINITION OF OUR METHOD

The corrupted image I can be expressed as the addition of the noise-free image s and noise η^*, i.e., $I=s+\eta^*$. For Gaussian noise, η^* satisfies the Gaussian distribution of zero mean and standard deviation of σ^*_η in the whole image. For speckle noise inherent in US imaging and SAR imaging, η^* will be described as $\eta^*=s^\gamma u$ where u is a zero-mean Gaussian random variable with a standard deviation of σ_u, and it is assumed to be stationary and independent of s [15], [37], [38]. A purely multiplicative noise with $\gamma=1$ has been considered for the US images [39], [40] and the SAR images [31], [41].

For the appreciation of restoration performance of the NLM method, the MSE has been widely adopted. However, the global MSE cannot reflect restoration performance at

an image pixel effectively. To address the problem of the automatic choice of the decay parameter for each image pixel, the pixel-wise MSE will be considered. The MSE at (x, y) is actually the local L_2 risk to measure the difference between the restored value $u(x, y)$ and $s(x, y)$, i.e., $\mathrm{MSE}[u(x,y)] = \mathbf{E}((u(x,y)-s(x,y))^2) = \mathbf{E}((u(x,y)-\mathbb{NL}[s](x,y)+\mathbb{NL}[s](x,y)-s(x,y))^2)$, where $\mathbf{E}$ denotes the expectation operator. Because η^* has zero mean and it is uncorrelated with s, the pixel-wise MSE can be decomposed into the sum of the squared bias $bias^2[u(x,y)]$ and the variance $var[u(x,y)]$.

$$\mathrm{MSE}[u(x,y)] = bias^2[u(x,y)] + var[u(x,y)], \tag{4}$$

where $bias^2[u(x,y)]$ and $var[u(x,y)]$ can be expressed as:

$$\begin{aligned} bias^2[u(x,y)] &= \mathbf{E}((\mathbb{NL}[s](x,y)-s(x,y))^2) \\ &= \left(\frac{\sum_{(p,q)\in\Omega} s(p,q)\omega(x,y,p,q)}{\sum_{(p,q)\in\Omega}\omega(x,y,p,q)} - s(x,y)\right)^2 \\ &= \left(\frac{\sum_{(p,q)\in\Omega} (s(p,q)-s(x,y))\omega(x,y,p,q)}{\sum_{(p,q)\in\Omega}\omega(x,y,p,q)}\right)^2 \end{aligned} \tag{5}$$

$$\begin{aligned} var[u(x,y)] &= \mathbf{E}((u(x,y) - \mathbb{NL}[s](x,y))^2) \\ &= \left(\frac{\sum_{(p,q)\in\Omega} (I(p,q) - s(p,q))\omega(x,y,p,q)}{\sum_{(p,q)\in\Omega}\omega(x,y,p,q)}\right)^2 \\ &= \left(\frac{\sum_{(p,q)\in\Omega} \eta^*(p,q)\omega(x,y,p,q)}{\sum_{(p,q)\in\Omega}\omega(x,y,p,q)}\right)^2 \end{aligned} \tag{6}$$

Obviously, $bias^2[u(x,y)]$ and $var[u(x,y)]$ are both relevant to h. To obtain the optimal decay parameter, $\mathrm{MSE}[u(x,y)]$ can be minimized with respect to h. However, $\mathrm{MSE}[u(x,y)]$ cannot be used in practice because $bias^2[u(x,y)]$ and $var[u(x,y)]$ in equations (5) and (6) are related to two unknown items s and η^*. A feasible solution to this problem is to use the optimal estimation results of s and η^* to approximate them.

Based on the above analysis, we have proposed the MSE based decay parameter adaptation scheme for the NLM method as shown in Fig. 1. In this scheme, the standard deviation of noise will be estimated firstly and it is utilized to generate the extended "noise patch". Based on the input noisy image and the extended "noise patch", the global MSE of the denoised image by the NLM method is minimized to obtain the globally optimal decay parameter h_{opt}. The global h_{opt} is used for the NLM method to produce the pre-denoised image. Based on the pre-denoised result and the corresponding method noise defined as the difference between the noisy image and its restored version, s and η^* are estimated by utilizing the residual image details in the method noise which are retrieved by the NLM method and the mean filter. The pixel-wise MSE is computed according to the estimated results of s and η^* and minimized to determine the optimal pixel-wise decay parameters h_{opt}, based on which the estimated denoised image is obtained and further processed using the boosting strategy to generate the final denoised image.

B. MINIMUM MSE BASED DECAY PARAMETER ADAPTATION

1) MINIMIZATION OF THE GLOBAL MSE

To restore s from I can be regarded as the problem of finding two components u and v which can approximate s and η^*, respectively, i.e., $I = u + v = s + \eta^*$, where v denotes the residual part of I. For the denoised result u, we can rewrite $\mathrm{MSE}[u]$ as:

$$\begin{aligned} \mathrm{MSE}[u] &= \mathbf{E}((u-s)^2) = var[u-s] + (\mathbf{E}(u-s))^2 \\ &= var[\eta^* - v] + (\mathbf{E}(\eta^* - v))^2 \\ &= var[\eta^* - v] + (\mathbf{E}(v))^2 \end{aligned} \tag{7}$$

We recall the identity $var[\eta^* - v] = var[\eta^*] + var[v] - 2cov[\eta^*, v]$, where $cov[\eta^*, v]$ denotes the covariance between η^* and v. Therefore, equation (7) is given by:

$$\mathrm{MSE}[u] = var[\eta^*] + var[v] - 2cov[\eta^*, v] + (\mathbf{E}(v))^2 \tag{8}$$

Based on the assumption that $var[\eta^* - v]$ and $E(v)$ are the smooth function related to h, the necessary condition for achieving the minimum $\mathrm{MSE}[u]$ will be expressed as:

$$\frac{\partial \mathrm{MSE}[u]}{\partial h} = \frac{\partial \mathrm{MSE}[u]}{\partial var[v]} \cdot \frac{\partial var[v]}{\partial h} = 0 \tag{9}$$

Because $\frac{\partial var[v]}{\partial h} \neq 0$ (see Appendix A for proof), it can be derived from equation (9) that the minimum $\mathrm{MSE}[u]$ can be achieved with the globally optimal decay parameter h_{opt} only if $\frac{\partial \mathrm{MSE}[u]}{\partial var[v]} = 0$. By computing the partial differential with respect to $var[v]$ on both sides of equation (8), we will obtain the following condition.

$$\frac{\partial cov[\eta^*, v]}{\partial var[v]} = \frac{1}{2} + \frac{\mathbf{E}(v) \cdot \partial \mathbf{E}(v)}{\partial var[v]} \tag{10}$$

However, this condition in equation (10) may not appear during the process of determining the global h_{opt}. To ensure that the signal and the noise are almost equally filtered so that the minimum $\mathrm{MSE}[u]$ can be achieved approximately, we will establish the function $f(h)$ related to h as:

$$f(h) = \left| \frac{\partial cov[\eta^*, v]}{\partial var[v]} - \frac{\mathbf{E}(v) \cdot \partial \mathbf{E}(v)}{\partial var[v]} - \frac{1}{2} \right| \tag{11}$$

By minimizing $f(h)$ in equation (11), h_{opt} can be obtained using such search algorithms as the golden section search method [42]. The minimization of $f(h)$ involves the computation of $\frac{\partial \mathbf{E}(v)}{\partial var[v]}$ and $\frac{\partial cov[\eta^*, v]}{\partial var[v]}$. The item $\frac{\partial \mathbf{E}(v)}{\partial var[v]}$ can be computed on the noisy image I. In order to approximate $cov[\eta^*, v]$ effectively, we refer to the direct estimation method proposed in [43]. In this method, we will simply extend I with a "noise patch" in one direction. In Figure 1, the extended "noise patch" of size 512×50 is shown for the input image I of size 512×512. Here, the "noise patch" is actually the sum of a constant (e.g., 120 in this paper) and the noise of variance $\tilde{\sigma}^2_{\eta^*}$, which is the estimated value of $\sigma^2_{\eta^*}$. The item $cov[\eta^*, v]$

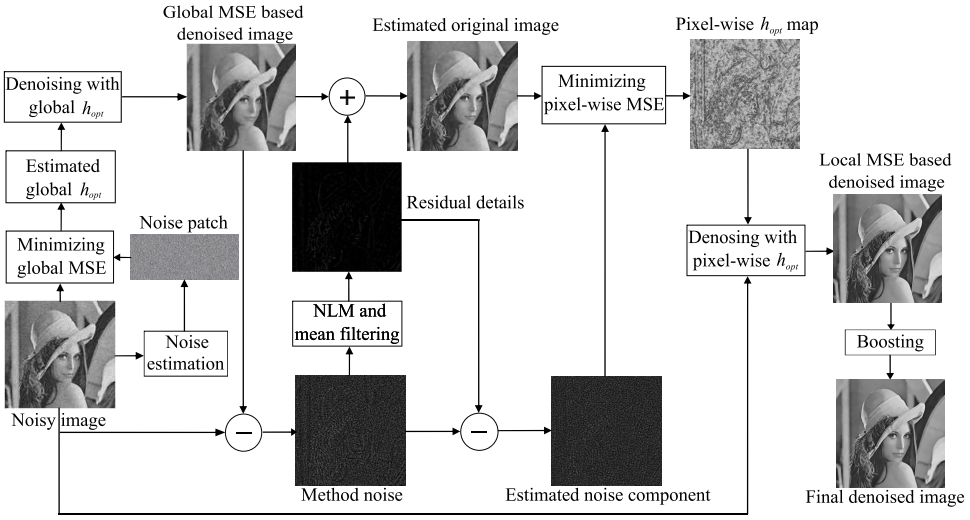

FIGURE 1. The proposed adaptive nonlocal means method for image denoising.

defined as $cov[\eta^*, v] = \mathbf{E}((\eta^* - \mathbf{E}(\eta^*))(v - \mathbf{E}(v)))$ is estimated on the extended "noise patch". For v in $cov[\eta^*, v]$, it will be calculated as the difference between the noise patch and its denoised result obtained by the NLM method using the considered decay parameter. For $\eta^* - \mathbf{E}(\eta^*)$, it can be easily computed based on the estimated noise of variance $\tilde{\sigma}^2_{\eta^*}$ which will be obtained in the following way.

For Gaussian noise, $\tilde{\sigma}_{\eta^*}$ is estimated using the median absolute deviation (MAD) based method [8]. For speckle noise, $\tilde{\sigma}_{\eta^*}$ will be estimated using the edge detection based method [36]. This method firstly creates a noisy image by subtracting from I a smooth version I_s obtained by a fast NLM method [44] and masking the edges in I_s by the Smallest Univalue Segment Assimilating Nucleus (SUSAN) edge detector [45]. Then the MAD based method is used on the created noisy image to estimate $\tilde{\sigma}_{\eta^*}$.

It should be noted that although the proposed global decay parameter adaptation based nonlocal means (GNLM) method is similar to the scheme presented in [43] in terms of the utilization of $\frac{\partial cov[\eta^*, v]}{\partial var[v]}$, our method differs from this work in two aspects. For one thing, the latter is focused on the optimal PDE-based denoising of Gaussian-noise corrupted images, but our method will be used for the optimal NLM denoising of both Gaussian-noise and speckle-noise corrupted images. On the other hand, $\frac{\mathbf{E}(v)\cdot\partial\mathbf{E}(v)}{\partial var[v]}$ has been considered additionally in our method. Because the imperfect image denoising will lead to the residual image details in v, there will exist the difference between the estimated noise component v and η^*, i.e., $\mathbf{E}(v) \neq 0$. By subtracting $\mathbf{E}(v)\cdot\partial\mathbf{E}(v)$ from $\partial cov[\eta^*, v]$, our method can attenuate the influence of the noise estimation error and thus can ensure the good restored results.

The GNLM algorithm involves several tuned parameters including the initial search range $[h_{min}, h_{max}]$ for the golden section search method and the interval Δh of the decay parameter for computing $\partial var[v]$. The search range can be chosen to be between 0 and a large value, but such a setting will reduce the computational efficiency. To ensure the efficient implementation of the GNLM method, we have performed extensive simulations on several standard test images corrupted with Gaussian noise and speckle noise of various variances to determine the distribution of h_{opt}. It is found that h_{opt} is almost in the range of $[0.5\tilde{\sigma}_{\eta^*}, \tilde{\sigma}_{\eta^*}]$ and $[0.95\tilde{\sigma}_{\eta^*}, 1.45\tilde{\sigma}_{\eta^*}]$ for Gaussian-noise and speckle-noise corrupted images, respectively. Correspondingly, this range will be set for $[h_{min}, h_{max}]$. For Δh, ideally, it should be set to be a relatively small value to ensure the effective computation of $\partial var[v]$. We have tested Δh in the range of [5, 25], and found that the GNLM method is very robust for the various images in this range. Therefore, $\Delta h = 10$ is chosen in this paper. The implementation of the GNLM method involves the following steps.

Step 1: Estimate the standard deviation $\tilde{\sigma}_{\eta^*}$ of noise in the noisy image I and extend I with the "noise patch" of the estimated $\tilde{\sigma}_{\eta^*}$.

Step 2: Initialize $\Delta h = 10$, and set the initial search range $[h_{min}, h_{max}]$ of the decay parameter for the golden section search method as $h^2_{min} = c\cdot\tilde{\sigma}^2_{\eta^*}$ and $h^2_{max} = (c+0.5)\cdot\tilde{\sigma}^2_{\eta^*}$ with the constant c chosen to be close to 0.5 and 0.95 for Gaussian noise and speckle noise, respectively.

Step 3: Determine two intermediate decay parameters h_1 and h_2 as $h_1 = h_{min} + 0.618\cdot(h_{max} - h_{min})$ and $h_2 = h_{max} - 0.618\cdot(h_{max} - h_{min})$.

Step 4: Calculate the denoised results u_1 and u'_1 of the image I for the NLM method using h_1 and $h_1 - \Delta h$ based on equation (1), respectively. Compute the corresponding noise components v_1 and v'_1 for I as $v_1 = I - u_1$ and $v'_1 = I - u'_1$. Compute the corresponding noise components v_2 and v'_2 for the "noise patch" in a similar way.

Step 5: Calculate $\partial var[v] = var[v_1] - var[v'_1]$ and $\partial\mathbf{E}(v) = \mathbf{E}(v_1) - E(v'_1)$ on the image I.

Step 6: Compute $\partial cov[\eta^*, v] = cov[\eta^*, v_2] - cov[\eta^*, v_2']$, where $cov[\eta^*, v_2]$ and $cov[\eta^*, v_2']$ are calculated on the ''noise patch''.

Step 7: Compute $f(h_1)$ and $f(h_2)$ according to equation (11).

Step 8: Update h_{max}, h_1 and h_2 as $h_{max} = h_1$, $h_1 = h_2$, and $h_2 = h_{max} - 0.618 \cdot (h_{max} - h_{min})$ while keeping h_{min} unchanged if $f[h_1] \geqslant f[h_2]$. Update h_{min}, h_1 and h_2 as $h_{min} = h_2$, $h_2 = h_1$, $h_1 = h_{min} + 0.618 \cdot (h_{max} - h_{min})$ while keeping h_{max} unchanged if $f[h_1] < f[h_2]$.

Step 9: If $h_{max} - h_{min} < \Delta h$, then stop the golden section search process, and output the optimal decay parameter as $h_{opt} = (h_{max} + h_{min})/2$ as well as the corresponding optimal denoised result $u_{h_{opt}}$. Otherwise, go to Step 3.

2) MINIMIZATION OF THE PIXEL-WISE MSE

In our study, it has been found that some residual details still exist in the method noise $v_{h_{opt}}$ ($v_{h_{opt}} = I - u_{h_{opt}}$). Thus the global MSE based denoised result $u_{h_{opt}}$ and $v_{h_{opt}}$ cannot provide the accurate estimation of s and η^*, respectively. To obtain the accurate denoised result, the residual image details will be extracted from $v_{h_{opt}}$ and utilized to estimate s and η^*.

Assuming that $v_{h_{opt}}$ comprises the complete noise component η^* and residual image details r, i.e., $v_{h_{opt}} = r + \eta^*$, the extraction of residual details can be regarded as the problem of denoising $v_{h_{opt}}$. Here, the NLM method will be adopted to address this problem. However, it will be difficult to retrieve r from $v_{h_{opt}}$ effectively if the weights in the NLM method are directly computed from $v_{h_{opt}}$ due to its low SNR. Considering that $v_{h_{opt}}$ is included in I, we resort to denoising $v_{h_{opt}}$ by the NLM method using the weights computed on I. Accordingly, r is expressed as:

$$\begin{aligned} r(x,y) &= \mathbb{NL}[v_{h_{opt}}](x,y) \\ &= \frac{\sum_{(p,q)\in\Omega} v_{h_{opt}}(p,q)\omega_{h_{opt}}(x,y,p,q)}{\sum_{(p,q)\in\Omega} \omega_{h_{opt}}(x,y,p,q)}, \end{aligned} \tag{12}$$

where $\omega_{h_{opt}}(x,y,p,q)$ is computed by replacing h in equation (2) with h_{opt} and further presented as:

$$\omega_{h_{opt}}(x,y,p,q) = \begin{cases} \omega_{h_{opt}}(x,y,p,q), & \text{if } \tilde{\omega}_{h_{opt}}(x,y,p,q) > T \\ 0, & \text{otherwise} \end{cases} \tag{13}$$

where $\tilde{\omega}_{h_{opt}}(x,y,p,q) = \frac{\omega_{h_{opt}}(x,y,p,q)}{\sum_{(p,q)\in\Omega} \omega_{h_{opt}}(x,y,p,q)}$ denotes the normalized weight; T ($0 \leq T < 1$) means the weight threshold used to dismiss the pixels with very low similarity weight from participating in the weighting averaging in the NLM method. An increasing T means that fewer pixels in the search window will be introduced into the filtering procedure. We have tested T in the range [0,0.02] and found that good denoised results can be obtained when T takes a value close to 0.0055.

Although the residual details can be extracted from the method noise by the NLM method, there is still some noise component in r. To remove the remaining noise, the mean filter with a 3×3 window ($\mathrm{MF}|_{3\times3}$) is adopted to provide good image detail preservation while delivering effective noise reduction. The estimated residual detail image $\hat{r}$ is presented as $\hat{r} = \mathrm{MF}[\mathbb{NL}[v_{h_{opt}}]]|_{3\times3}$. Based on $\hat{r}$, the estimated original image $\hat{s}$ and noise $\hat{\eta^*}$ are computed as $\hat{s} = u_{h_{opt}} + \hat{r}$ and $\hat{\eta^*} = v_{h_{opt}} - \hat{r}$.

With $\hat{s}$ and $\hat{\eta^*}$, the cost function $J[h(x,y)]$ related to $h(x,y)$ is derived as the improved version of the estimated pixel-wise MSE to guide the determination of the decay parameter, i.e., $J[h(x,y)] = \hat{bias}^2[u(x,y)] + \hat{var}[u(x,y)]$. Here, the estimated squared bias $\hat{bias}^2[u(x,y)]$ and variance $\hat{var}[u(x,y)]$ are computed based on equations (5) and (6) by replacing s with $\hat{s}$ and η^* with $\hat{\eta^*}$, i.e.,

$$\hat{bias}^2[u(x,y)] = \left(\frac{\sum_{(p,q)\in\Omega} (\hat{s}(p,q) - \hat{s}(x,y))\hat{\omega}(x,y,p,q)}{\sum_{(p,q)\in\Omega} \hat{\omega}(x,y,p,q)} \right)^2, \tag{14}$$

$$\hat{var}[u(x,y)] = \left(\frac{\sum_{(p,q)\in\Omega} \hat{\eta^*}(p,q)\hat{\omega}(x,y,p,q)}{\sum_{(p,q)\in\Omega} \hat{\omega}(x,y,p,q)} \right)^2, \tag{15}$$

where the weight $\hat{\omega}(x,y,p,q)$ is computed on $\hat{s}$ instead of I to attenuate the disadvantageous influence of noise.

It is easy to understand that the optimal pixel-wise decay parameter can be obtained when $J[h(x,y)]$ achieves the minimum. Therefore, $J[h(x,y)]$ is optimized iteratively using the steepest descent method to produce $h(x,y)$ as:

$$h^{n+1}(x,y) = h^n(x,y) - \alpha \frac{\partial J[h^n(x,y)]}{\partial h(x,y)} \tag{16}$$

where α is the step size. The term $\frac{\partial J[h(x,y)]}{\partial h(x,y)}$ is computed as:

$$\frac{\partial J[h(x,y)]}{\partial h(x,y)} = \left(\frac{\partial \hat{bias}^2[u(x,y)]}{\partial h(x,y)} + \frac{\partial \hat{var}[u(x,y)]}{\partial h(x,y)} \right) \tag{17}$$

where the derivation of the two items $\frac{\partial \hat{bias}^2[u(x,y)]}{\partial h(x,y)}$ and $\frac{\partial \hat{var}[u(x,y)]}{\partial h(x,y)}$ can be found in Appendix B.

The local MSE based denoised image Y will be obtained by the NLM method, where the weights produced from the optimal pixel-wise decay parameters are thresholded by the weight threshold T_1 as done in equation (13). Considering that the residual noise may still remain and some details may be lost in Y, the boosting strategy proposed for K-SVD denoising in [46] will be adopted. In the boosting scheme, the denoised image Y is firstly added to I to produce the strengthened image S, and then S is denoised by the pixel-wise adaptive NLM method. Finally, Y is subtracted from the restored signal-strengthened result to produce the final denoised image F. This procedure can be be expressed as:

$$S(x,y) = I(x,y) + \beta Y(x,y), \tag{18}$$

$$F(x,y) = \mathbb{NL}[S](x,y) - \beta Y(x,y), \tag{19}$$

where β denotes a constant, and $\mathbb{NL}[S](x, y)$ is the denoised result by the NLM method, where the weights are computed using the obtained distance between image patches in the image $\hat{s}$ and the decay parameter $h'(x, y)$ ($h'(x, y) = \beta h_{opt}(x, y)$) and then thresholded by T_1.

The pixel-wise decay parameter adaptation based nonlocal means (PNLM) consists of the following steps.

Step 1: Obtain the residual detail image $\hat{r}$ by implementing the NLM method on the method noise $v_{h_{opt}}$ and the mean filter on the $\mathbb{NL}[v_{h_{opt}}]$. Estimate the original image and noise as $\hat{s} = u_{h_{opt}} + \hat{r}$ and $\hat{\eta}^* = v_{h_{opt}} - \hat{r}$.

Step 2: Set the maximum iteration times $n_{max} = 60$ and $T = 0.0055$. Set $T_1 = 0.003$, $h^0(x, y) = 6\tilde{\sigma}_{\eta^*}$ and $\alpha = 6$ for the Gaussian-noise corrupted image while $T_1 = 0.002$, $h^0(x, y) = 4.5\tilde{\sigma}_{\eta^*}$ and $\alpha = 0.25$ for the speckle-noise corrupted image.

Step 3: Initialize the iteration times $n = 0$.

Step 4: Compute $\frac{\partial J[h^n(x,y)]}{\partial h(x,y)}$ for the pixel at (x, y) according to equation (17).

Step 5: Update the decay parameter $h^{n+1}(x, y)$ using equation (16).

Step 6: If $n = n_{max}$ or $||\frac{\partial J[h^n(x,y)]}{\partial h(x,y)}|| < \varepsilon$ ($\varepsilon = 10^{-4}$), then stop the iteration process for the considered pixel, output the optimal pixel-wise decay parameter as $h_{opt}(x, y) = h^{n+1}(x, y)$ as well as the corresponding optimal denoised result, and go to step 7. Otherwise, $n = n + 1$ and go to step 4.

Step 7: If all image pixels have been processed, then stop the PNLM method to generate the estimated denoised image Y. Otherwise, process the next image pixel and go to step 3.

Step 8: Set β to be close to 0.85 and implement the boosting strategy on the image Y according to equations (18) and (19) to generate the final denoised image.

III. EXPERIMENTAL RESULTS AND DISCUSSIONS

In this section, we will firstly verify the effectiveness of the proposed GNLM and PNLM methods in determining the optimal decay parameter. Then, experiments are done on some standard 512×512 grayscale and color images, and two texture images Straw and Brickwall shown in Fig. 2 as well as three real images to appreciate restoration performance of our method. Finally, the computational efficiency of our method is discussed.

A. ANALYSIS OF THE GNLM AND PNLM METHODS

To verify that the GNLM method can determine h_{opt} effectively, we will test different h on the standard images. Fig. 3 shows the MSE curves of the denoised results for the Lena, Barbara and Airplane images corrupted by Gaussian noise with $\sigma_{\eta^*} = 40$ and speckle noise with $\sigma_u = 0.3$. The black curves, ★ and ▼ denote the MSE values resulting from using different h, the estimated and real minimum ones, respectively. From Fig. 3, we can see that the estimated h_{opt} values are close to the real ones, and thus there only exist the small differences between the estimated minimum MSE values and the real ones for the different Gaussian-noise and speckle-noise corrupted images.

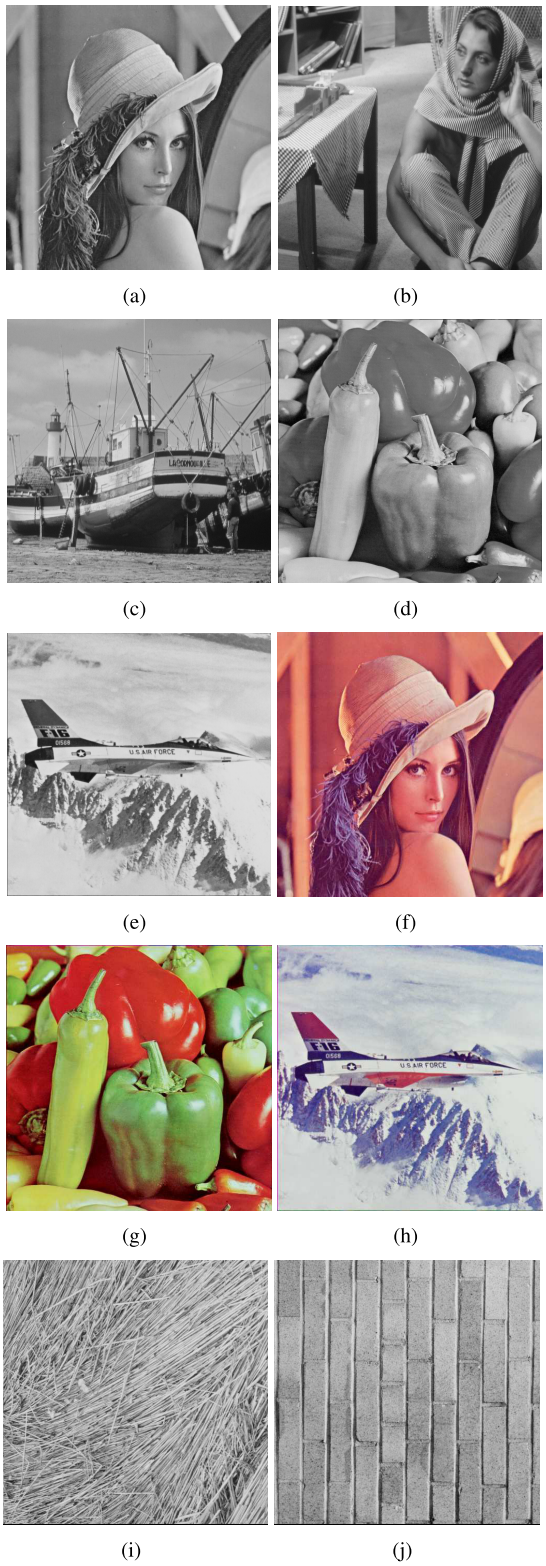

FIGURE 2. Standard grayscale and color images, and texture images. (a)-(e) Grayscale Lena, Barbara, Boat, Peppers and Airplane images, respectively. (f)-(h) Color Lena, Peppers and Airplane images, respectively. (i)-(j) Straw and Brickwall images, respectively.

Furthermore, the differences between the estimated optimal pixel-wise decay parameters and the ideal ones for the Lena, Barbara and Peppers images are shown in Fig. 4.

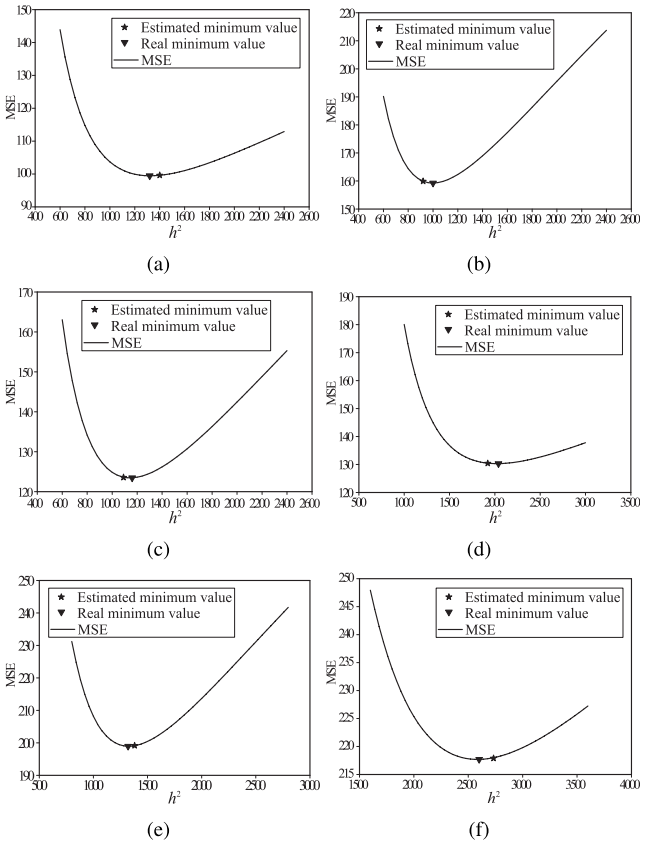

FIGURE 3. The MSE curve, the estimated and real minimum MSE for the GNLM method operating on the three images. (a)-(c) MSE for the Gaussian-noise corrupted Lena, Barbara and Airplane images with $\sigma_{\eta*} = 40$, respectively. (d)-(f) MSE for the speckle-noise corrupted Lena, Barbara and Airplane images with $\sigma_u = 0.3$, respectively.

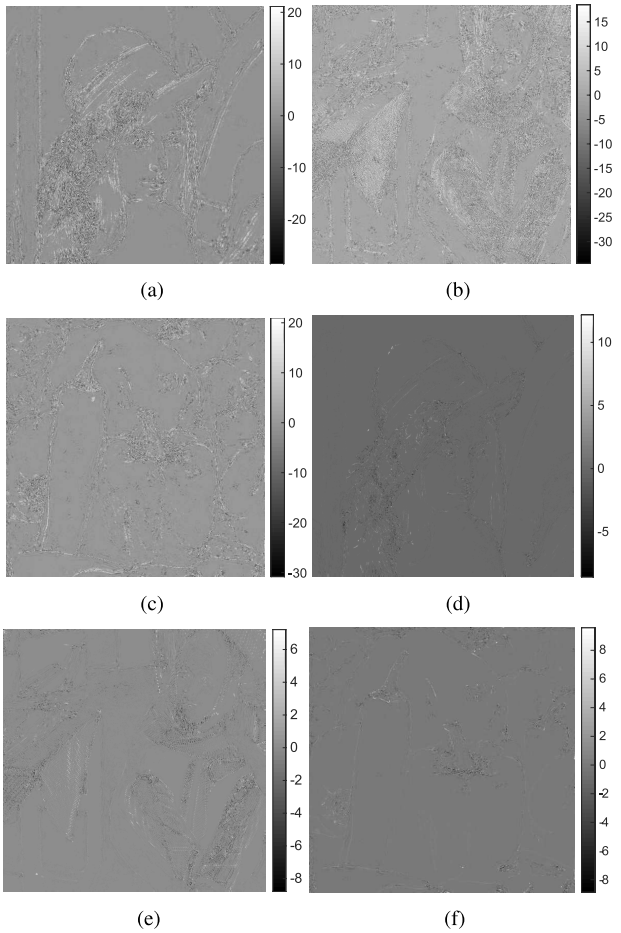

FIGURE 4. The differences between the estimated pixel-wise decay parameters and the ideal ones for the PNLM method operating on the Lena, Barbara and Peppers images. (a)-(c) The differences for the three Gaussian-noise corrupted images with $\sigma_{\eta*} = 40$. (d)-(f) The differences for the three speckle-noise corrupted images with $\sigma_u = 0.3$.

Here, the ideal decay parameters for each image are obtained by minimizing $J[h(x, y)]$ where $\hat{s}$ and $\hat{\eta}^*$ are replaced with s and η^*, respectively. As shown in Fig. 4, the differences of pixel-wise decay parameters are very small in the smooth regions, which will facilitate sufficient noise suppression by the PNLM method. In the edge regions, there exist some differences of decay parameters because the complicated image details will lead to the inaccurate estimation of the original image and the noise component. However, the involved differences in these regions are generally small, which can ensure the effective preservation of image details by the proposed method.

B. EXPERIMENTS ON THE GRAYSCALE IMAGES

For Gaussian noise, restoration performance will be compared among the traditional NLM method using a fixed decay parameter with $h = \hat{\sigma}_{\eta^*}$ [5], the SURE method [34], the PSURE method [35], the C_p-NLM method [36], the BM3D method [12], the denoising convolutional neural network (DnCNN) based method [6], the GNLM method and the PNLM method. For speckle noise, considering that the SURE and PSURE methods are not suitable for speckle reduction, we have chosen the NLM method, the probabilistic patch-based (PPB) filter [15], the optimized Bayesian nonlocal means (OBNLM) method [17], the BM3D method and the DnCNN method for comparisons with our methods. In the proposed methods, the 17×17 search window is selected, and the 9×9 and 25×25 similarity windows are chosen for the GNLM method and the PNLM method, respectively. For all compared NLM methods, to ensure a good trade-off between computational efficiency and restoration performance, we have fixed the search window and the similarity window to be 17×17 and 9×9, respectively. It should be noted that for the BM3D method, the parameters of the ''Normal Profile'' suggested in [12] are used except that the search window of size 17×17 instead of 39×39 is used to make a fair comparison with the proposed method. Meanwhile, the BM3D has been implemented for once and three times to suppress Gaussian noise and speckle noise, respectively. The parameters in the DnCNN method are chosen as suggested in [6] except that this method is trained on 200 images chosen from the dataset released at [47] for 20 epochs.

TABLE 1. Comparison of PSNR (*dB*)/SSIM for the various methods operating on five standard images corrupted by Gaussian noise with different standard deviations.

Images	σ_{η^*}	/	NLM	SURE	PSURE	C_p-NLM	BM3D	DnCNN	GNLM	PNLM
Lena	20	22.10/0.678	31.72/0.912	31.98/0.919	32.22/0.924	32.10/0.921	33.18/0.938	**33.36**/0.939	31.99/0.920	33.26/**0.940**
	30	18.57/0.531	29.59/0.873	29.68/0.877	30.21/0.889	30.05/0.884	31.29/0.909	31.41/0.911	29.72/0.878	**31.52/0.914**
	40	16.09/0.431	28.14/0.837	28.18/0.838	28.76/0.858	28.57/0.849	29.74/0.878	30.04/0.886	28.20/0.838	**30.20/0.887**
	50	14.15/0.354	26.94/0.800	26.95/0.800	27.60/0.824	27.16/0.819	28.64/0.853	29.03/0.858	26.96/0.800	**29.19/0.863**
Barbara	20	22.10/0.764	30.00/0.924	30.24/0.934	30.75/0.938	30.25/0.930	**31.35**/0.946	30.59/0.942	30.36/0.934	31.11/**0.947**
	30	18.60/0.630	27.52/0.875	27.94/0.890	28.64/0.906	28.00/0.888	29.33/0.918	28.14/0.902	28.01/0.890	**29.35/0.919**
	40	16.10/0.525	25.66/0.826	26.20/0.843	27.05/0.864	26.18/0.845	27.40/0.882	26.20/0.860	26.23/0.844	**27.76/0.886**
	50	14.12/0.440	24.49/0.780	24.78/0.793	25.78/0.826	24.92/0.801	26.67/**0.862**	24.83/0.819	24.79/0.793	**26.68**/0.854
Boat	20	22.12/0.702	29.93/0.900	30.32/0.917	30.45/0.919	30.42/0.915	31.49/0.941	**31.77/0.943**	30.36/0.915	31.28/0.936
	30	18.57/0.564	27.74/0.848	28.19/0.861	28.43/0.876	28.30/0.866	29.50/0.904	**29.82/0.911**	28.21/0.862	29.44/0.906
	40	16.07/0.467	26.24/0.800	26.52/0.809	26.93/0.833	26.80/0.821	28.04/0.867	**28.40/0.876**	26.67/0.813	28.16/0.869
	50	14.12/0.394	25.18/0.760	25.32/0.764	25.85/0.797	25.71/0.792	26.90/0.840	**27.38/0.841**	25.35/0.765	27.17/0.836
Peppers	20	22.11/0.667	31.74/0.927	31.81/0.929	32.11/0.932	32.00/0.931	32.74/0.941	**32.90**/0.941	31.84/0.929	32.57/**0.942**
	30	18.59/0.517	29.83/0.898	29.85/0.898	30.43/0.905	30.15/0.901	31.18/0.919	**31.38**/0.920	29.88/0.898	31.26/**0.921**
	40	16.10/0.415	28.38/0.866	28.40/0.867	29.19/0.881	28.67/0.876	29.84/0.894	30.07/0.897	28.39/0.866	**30.14/0.903**
	50	14.16/0.340	27.10/0.837	27.12/0.837	28.10/0.859	27.32/0.845	28.62/0.875	29.02/0.876	27.11/0.838	**29.07/0.881**
Airplane	20	22.12/0.654	31.15/0.920	31.40/0.925	31.26/0.925	31.50/0.926	32.26/0.939	**32.74/0.942**	31.34/0.924	32.19/0.940
	30	18.59/0.516	28.76/0.884	28.97/0.884	29.22/0.894	29.40/0.896	30.34/0.913	**30.75**/0.914	29.05/0.885	30.36/**0.915**
	40	16.10/0.425	26.93/0.844	27.19/0.843	27.78/0.865	27.70/0.864	28.73/0.884	**29.21**/0.889	27.21/0.841	29.00/**0.893**
	50	14.16/0.358	25.60/0.805	25.79/0.803	26.62/0.835	26.52/0.834	27.62/0.862	**28.12**/0.868	25.80/0.804	27.92/**0.870**

TABLE 2. Comparison of PSNR (*dB*)/SSIM for the various methods operating on the five standard images corrupted by speckle noise with different standard deviations.

Images	σ_u	/	NLM	PPB	OBNLM	C_p-NLM	BM3D	DnCNN	GNLM	PNLM
Lena	0.2	19.64/0.608	29.47/0.868	30.03/0.868	30.42/0.895	29.56/0.869	30.88/0.907	**32.36/0.920**	29.52/0.869	31.98/0.912
	0.3	16.11/0.482	27.01/0.806	28.32/0.836	27.88/0.833	27.10/0.810	28.55/0.853	**30.25**/0.874	27.05/0.807	30.11/**0.876**
	0.4	13.60/0.394	25.25/0.747	26.36/0.775	26.21/0.777	25.56/0.756	27.40/0.820	**28.71**/0.832	25.43/0.753	28.65/**0.842**
Barbara	0.2	19.84/0.727	27.66/0.880	28.38/0.890	28.56/0.915	28.03/0.889	28.90/0.914	29.15/0.916	27.76/0.888	**29.29/0.918**
	0.3	16.35/0.601	25.04/0.811	25.85/0.828	26.02/0.854	25.14/0.820	26.42/0.856	26.38/0.862	25.06/0.818	**27.27/0.867**
	0.4	13.81/0.505	23.24/0.742	24.20/0.765	24.40/0.802	23.40/0.752	25.30/0.805	24.61/0.812	23.21/0.749	**25.61/0.816**
Boat	0.2	18.82/0.613	27.69/0.845	28.31/0.853	28.55/0.872	27.92/0.855	29.09/0.895	**30.34/0.905**	27.94/0.853	29.67/0.896
	0.3	15.32/0.492	25.44/0.768	26.01/0.782	26.25/0.798	25.35/0.768	27.06/0.831	**28.31/0.851**	25.46/0.771	27.84/0.849
	0.4	12.79/0.414	23.83/0.697	24.58/0.726	24.60/0.727	23.94/0.703	25.91/0.799	**26.90/0.813**	23.80/0.695	26.55/0.803
Peppers	0.2	19.21/0.586	29.50/0.891	30.20/0.905	30.09/0.902	29.71/0.892	30.80/0.916	**31.70**/0.917	29.60/0.894	31.32/**0.918**
	0.3	15.66/0.454	27.07/0.839	28.20/0.867	27.70/0.852	27.27/0.843	28.97/0.885	**29.90**/0.885	27.18/0.845	29.63/**0.891**
	0.4	13.18/0.365	25.32/0.788	26.44/0.830	26.64/0.802	25.45/0.802	27.56/0.847	28.30/0.843	25.44/0.800	**28.32/0.862**
Airplane	0.2	16.76/0.461	27.25/0.837	28.32/0.869	28.33/0.858	27.42/0.845	29.10/0.882	**30.28**/0.885	27.52/0.844	29.81/**0.898**
	0.3	13.23/0.358	24.62/0.754	26.00/0.797	25.92/0.784	24.80/0.760	27.12/0.837	27.94/0.826	24.76/0.757	**28.21/0.860**
	0.4	10.75/0.291	22.99/0.670	24.02/0.721	24.11/0.703	23.25/0.683	25.22/0.770	26.21/0.789	23.03/0.680	**26.22/0.801**

For the quantitative appreciation of restoration performance, we will use such indexes as PSNR and SSIM [48] which are defined as:

$$\mathrm{PSNR}[F] = 10\log_{10}\left(\frac{255^2}{\mathrm{MSE}[F]}\right), \tag{20}$$

$$\mathrm{SSIM}[F] = \frac{(2\bar{s}\bar{F} + C_1)(2\delta_{sF} + C_2)}{(\bar{s}^2 + \bar{F}^2 + C_1)(\delta_s^2 + \delta_F^2 + C_2)}, \tag{21}$$

where $\bar{s}$ and $\bar{F}$ are the mean of s and F, respectively; δ_s and δ_F are the standard deviation of s and F, respectively; δ_{sF} is the covariance between s and F; C_1 and C_2 are the small constants to stabilize SSIM and chosen as $C_1 = (K_1L)^2$ and $C_2 = (K_2L)^2$, where L is the observed dynamic range, $K_1 = 0.01$ and $K_2 = 0.03$. It should be noted that the SSIM is computed locally based on the automatic downsampling as suggested at [49].

Tables 1 and 2 list PSNR and SSIM of all evaluated methods operating on the five grayscale images corrupted by Gaussian noise and speckle noise, respectively. Fig. 5 shows the mean PSNR for each evaluated method.

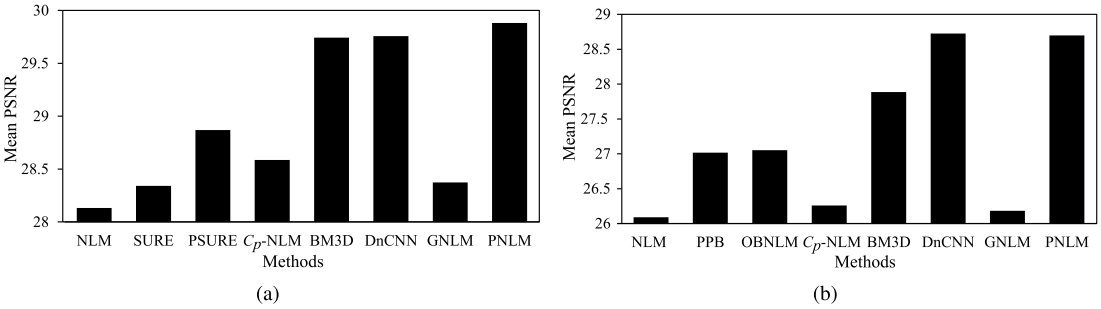

FIGURE 5. The mean PSNR for each evaluated method operating on the five standard images corrupted with Gaussian noise and speckle noise. (a) Gaussian noise. (b) Speckle noise.

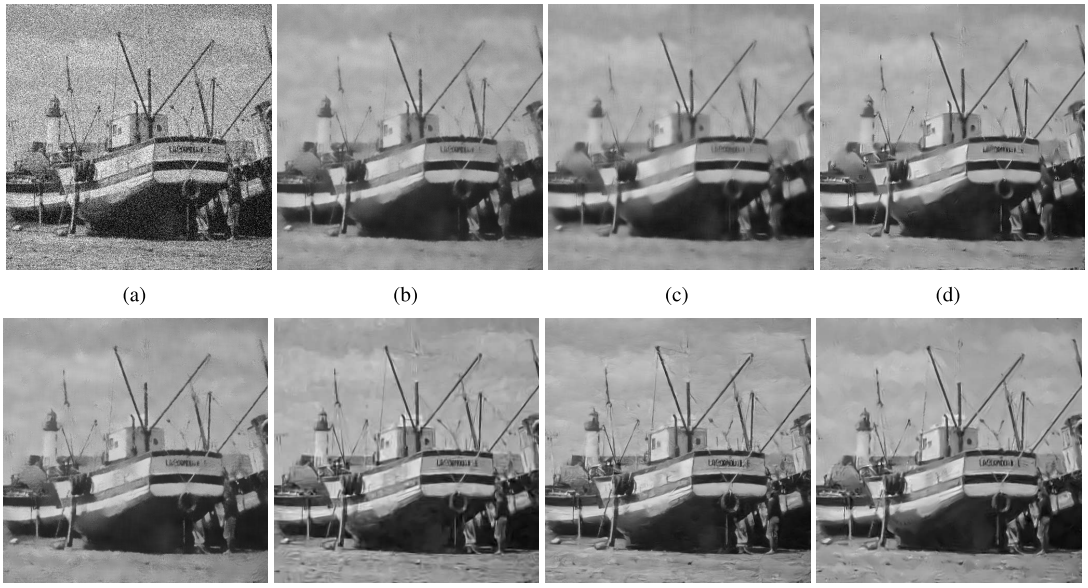

FIGURE 6. Comparisons of restored results for the various denoising methods operating on the Boat image corrupted with Gaussian noise of $\sigma_{\eta^*} = 40$. (a) Noisy ROI. (b) NLM. (c) SURE. (d) PSURE. (e) C_p-NLM. (f) BM3D. (g) DnCNN. (h) PNLM.

Obviously, the PSNR and SSIM values of the PNLM method are much higher than those of the NLM method and the GNLM method, which indicates the advantage of the pixel-wise decay parameter adaptation strategy over the strategy of using the globally fixed parameter. Compared with the pixel-wise adaptive NLM methods, the PNLM method, on average, provides approximate PSNR improvements of 1 dB and 1.28 dB over the PSURE and C_p-NLM methods as shown in Fig. 5(a), respectively. Fig. 5(b) shows that the mean PSNR improvements provided by the PNLM method over the C_p-NLM, PPB and OBNLM methods almost amount to 2.43 dB, 1.68 dB and 1.65 dB, respectively. Compared with the BM3D, the proposed method provides higher PSNR and SSIM values for Gaussian noise removal in most cases and speckle noise reduction in all cases. The DnCNN method performs unsatisfactorily in denoising the Barbara image. Although this method provides higher PSNR values in some cases, it produces lower SSIM values than the PNLM method in most cases, which indicates the superiority of the proposed PNLM method over the DnCNN method in preserving image details.

Fig. 6 shows the visual impression of all evaluated methods for the Boat image corrupted by Gaussian noise with $\sigma_{\eta^*} = 40$. Fig. 7 shows the comparisons of the enlarged view of regions of interest (ROIs) chosen from Fig. 6 to further demonstrate the advantage of the proposed method. It can be seen from Fig. 6 and Fig. 7 that the NLM method and the SURE method lead to obvious image over-smoothing due to the adoption of the globally fixed decay parameter. The PSURE and C_p-NLM methods can preserve some image details better than the above two methods by using the pixel-wise adaptive decay parameters, but they remain some noise in the denoised results. The BM3D method cannot preserve the fine details and introduce some unwanted artifacts as showed by the three white boxes, and it performs worse in maintaining the sharpness of image details than the PNLM method. Compared with the DnCNN method, the proposed method can preserve the integrity of edges better and produce

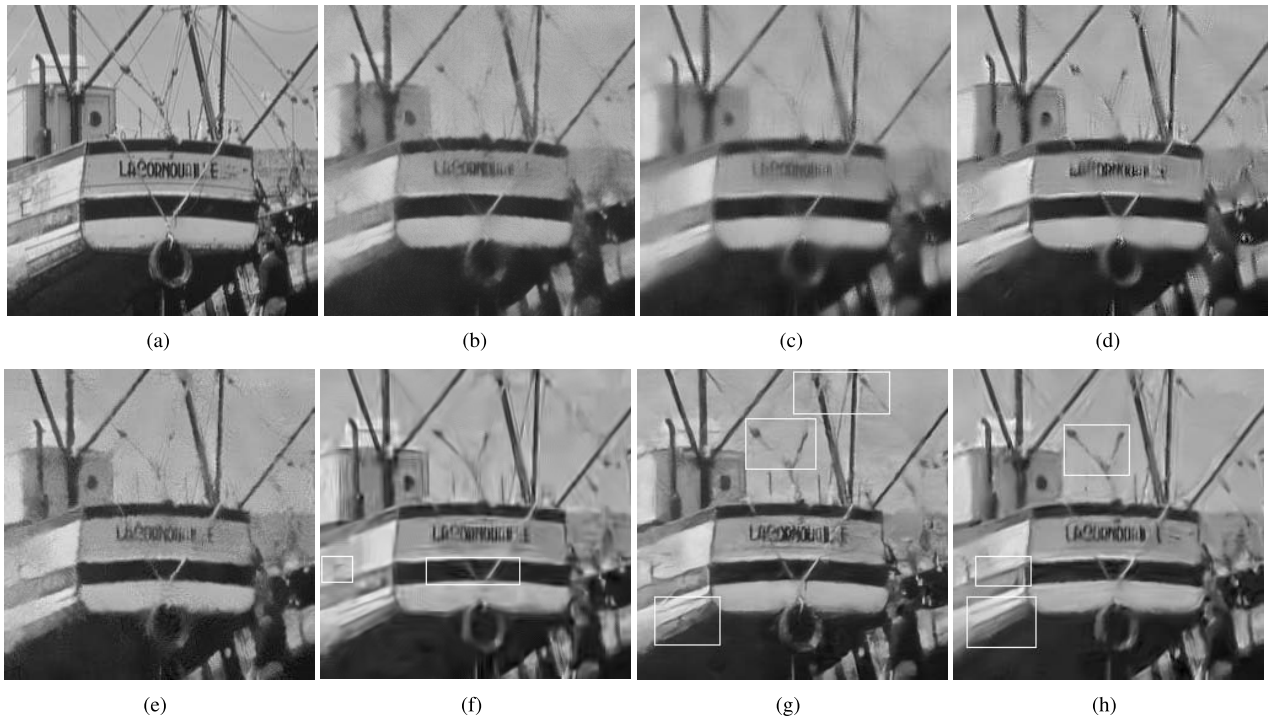

FIGURE 7. Enlarged view of the ROIs in the restored results shown in Fig. 6. (a) Original ROI. (b) NLM. (c) SURE. (d) PSURE. (e) C_p-NLM. (f) BM3D. (g) DnCNN. (h) PNLM.

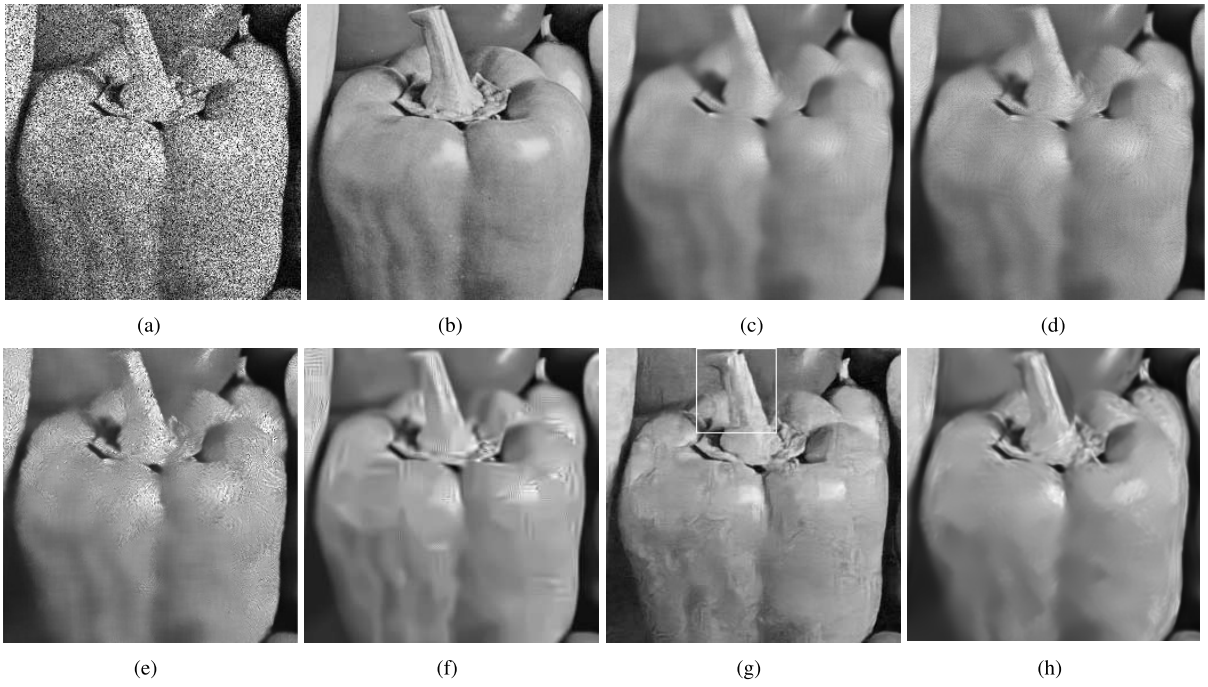

FIGURE 8. Enlarged view of the ROIs in the restored results for the evaluated methods operating on the Peppers image corrupted with speckle noise of $\sigma_u = 0.4$. (a) Noisy ROI. (b) Original ROI. (c) PPB. (d) OBNLM. (e) C_p-NLM. (f) BM3D. (g) DnCNN. (h) PNLM.

less distortion of image edges as indicated by the three white boxes.

Fig. 8 shows the enlarged view of ROIs chosen from the restored results of the Peppers image corrupted by speckle noise with $\sigma_u = 0.4$. Clearly, the PPB and OBNLM methods suppress speckle noise effectively but result in over-smoothing of image details. The C_p-NLM method remains some speckle noise in the restored results.

(a) (b) (c) (d)

FIGURE 9. Denoised results of BM3D and PNLM methods operating on the color Lena image corrupted with Gaussian noise of $\sigma_{\eta^*} = 40$. (a) Noisy image. (b) Original image. (c) BM3D. (d) PNLM.

TABLE 3. Comparison of PSNR (*dB*)/SSIM for the BM3D and PNLM methods operating on the two texture images corrupted by Gaussian noise.

Methods	Straw		Brickwall	
	$\sigma_{\eta^*} = 30$	$\sigma_{\eta^*} = 40$	$\sigma_{\eta^*} = 30$	$\sigma_{\eta^*} = 40$
BM3D	24.76/0.920	22.82/0.859	**26.59**/0.779	**25.82**/0.742
PNLM	**24.90/0.927**	**23.27/0.874**	26.48/**0.781**	25.78/**0.745**

The BM3D method introduces obvious unwanted artifacts. The DnCNN method damages some weak image details as shown by the white box. By comparison, the PNLM method delivers sufficient speckle noise reduction while preserving some details very well.

C. EXPERIMENTS ON THE TEXTURE IMAGES

To demonstrate the advantage of the PNLM method in denoising the corrupted texture images, we will test our method on Straw and Brickwall images shown in Figure 2. The two images are from the Brodatz texture images avaliable at http://sipi.usc.edu/database/database.php?volume=textures. The restoration performance of the PNLM method is compared with that of the BM3D method. Table 3 shows the PSNR and SSIM of the two methods for the Gaussian-noise corrupted images. It can be seen that compared with the BM3D method, the proposed PNLM method can provide higher PSNR and SSIM in restoring the corrupted Straw image and competitive PSNR and SSIM for the Brickwall image.

D. EXPERIMENTS ON THE COLOR IMAGES

The RGB color Lena, Peppers and Airplane images corrupted with Gaussian noise of $\sigma_{\eta^*} = 40$ and speckle noise of $\sigma_u = 0.3$ are used to appreciate the effectiveness of the PNLM method. Similar to [12], these color images are transformed into the luminance and chrominance channels using the opponent color transformations. Denoising is done separately on each transformed channel.

Table 4 lists the PSNR and SSIM of the BM3D and PNLM methods. The observation from Table 3 shows that the PNLM method provides higher PSNR and SSIM than the BM3D method in most cases. Fig. 9 shows the denoised results of the two methods operating on the Lena image corrupted with Gaussian noise of $\sigma_{\eta^*} = 40$. The visual comparisons clearly demonstrate that the BM3D method will remain some noise in the denoised image while the PNLM method can remove Gaussian noise from the image more effectively.

(a) (b) (c)

FIGURE 10. Three real images. (a) MR image (224×260). (b) SAR image (340×340). (c) US image (328×312).

E. APPLICATION TO REAL IMAGE DENOISING

The proposed method is also applied to denoising a real brain magnetic resonance (MR) image available at [51], a SAR image [52] (Courtesy of Sandia National Laboratories, Radar ISR) and a liver US image acquired by our lab. These images are shown in Fig. 10. It has been well known that the Rician noise in the MR image with high SNR can be approximated to be Gaussian one [50] and the noise in the SAR and US images is generally regarded as multiplicative speckle noise. Thus, the proposed method can be used for denoising the three images. To appreciate restoration performance of various denoising methods operating on these images, we will use such no-reference metrics as contrast-to-noise ratio (CNR) and SNR [53] defined as:

$$\text{CNR} = \frac{|\hat{\mu}_o - \hat{\mu}_b|}{\hat{\sigma}_b} \tag{22}$$

$$\text{SNR} = \frac{\hat{\mu}_b}{\hat{\sigma}_b} \tag{23}$$

where $\hat{\mu}_o$ is the mean intensity of pixels in the object, $\hat{\mu}_b$ and $\hat{\sigma}_b$ denote the mean intensity and the standard deviation of noise in the background surrounding the object, respectively.

Three pairs of ROIs marked by different colors are selected from Fig. 10. Table 5 lists the CNR and SNR for each

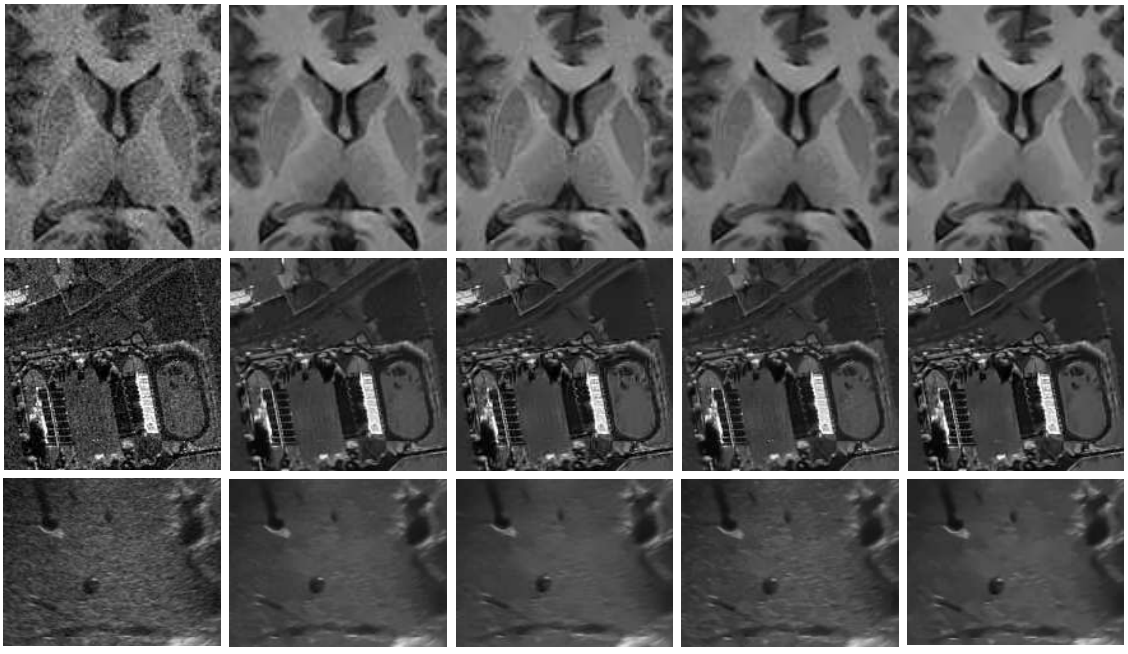

FIGURE 11. Visual comparisons of the restored results of the three chosen ROIs for the evaluated denoising methods. (a) From top to bottom: ROIs chosen from MR, SAR and US images. (b) NLM. (c) From top to bottom: PSURE, PPB and OBNLM. (d) C_p-NLM. (e) PNLM.

TABLE 4. Comparison of PSNR (*dB*)/SSIM for the BM3D and PNLM methods operating on the three color images corrupted by Gaussian noise and speckle noise.

Methods	Lena		Peppers		Airplane	
	$\sigma_{\eta^*} = 40$	$\sigma_u = 0.3$	$\sigma_{\eta^*} = 40$	$\sigma_u = 0.3$	$\sigma_{\eta^*} = 40$	$\sigma_u = 0.3$
BM3D	29.80/0.881	28.98/**0.873**	29.10/0.869	28.19/0.872	**29.88**/0.897	**28.52/0.869**
PNLM	**29.99/0.886**	**29.33**/0.867	**29.19/0.878**	**28.86/0.878**	29.77/**0.904**	28.36/0.852

TABLE 5. Comparison of SNR (*dB*)/CNR for the various methods operating on the three real images.

Image	ROIs	Noisy ROI	NLM	PSURE	C_p-NLM	PNLM
MR	Black window	9.98/5.35	31.53/16.88	27.92/14.91	30.40/16.24	**43.05/23.05**
	Blue window	7.03/3.29	10.38/4.77	9.52/4.39	10.42/4.78	**10.66/4.91**
	White window	2.72/4.25	13.19/20.86	9.75/15.56	12.30/19.57	**21.68/33.98**
Image	ROIs	Noisy ROI	NLM	PPB	C_p-NLM	PNLM
SAR	Black window	2.85/0.72	8.67/2.18	8.99/2.27	7.80/1.97	**9.30/2.40**
	Blue window	3.44/1.36	12.99/4.92	13.86/5.41	11.66/4.57	**14.09/5.45**
	White window	4.22/1.33	9.72/2.91	8.51/2.61	9.27/2.81	**9.79/2.94**
Image	ROIs	Noisy ROI	NLM	OBNLM	C_p-NLM	PNLM
US	Black window	4.34/0.80	13.63/2.28	13.97/2.46	10.69/1.85	**14.45/2.63**
	Blue window	5.58/0.072	16.04/0.160	17.55/0.176	11.93/0.118	**17.70/0.226**
	White window	4.99/2.60	13.89/6.85	14.29/7.08	9.79/4.96	**15.03/7.63**

evaluated method. Clearly, the PNLM method provides higher CNR and SNR than the compared methods. Fig. 11 shows the denoised results of three ROIs for these methods. Obviously, the other methods cannot maintain the sharpness of regions of brain gyri and sulci in the MR image, buildings and streets in the SAR image and vessels in the US image, and cannot suppress noise superimposed in these regions effectively. By comparison, the PNLM method can suppress speckle noise and preserve the edges in these regions very well.

F. COMPUTATIONAL COMPLEXITY

In the proposed GNLM and PNLM methods, the computation of the distance between image patches is most time-consuming. To address this issue, the fast distance computation method proposed in [44] is utilized here, and no repetitive distance computation will be done for determining the global and pixel-wise decay parameters by computing the distances only once in advance and then calling them for the decay parameter optimization. Apart from the distance computation, the golden search method in the GNLM method and the steepest descent method in the PNLM method will influence the efficiency of our method. In this paper, a small initial search range for this search method and relatively few iteration times for the steepest descent method have been chosen to ensure the computational efficiency. Based on the above strategy, we have implemented the proposed method with MATLAB 2013b on the computer with 3.0 GHz CPU and 64GB RAM. By using the fast distance computation strategy, the mean execution time for the NLM, GNLM and PNLM methods operating on the five Gaussian-noise corrupted grayscale images is 18 seconds, 118 seconds and 480 seconds, respectively. Clearly, the proposed methods are slower than the NLM method. The parallel computation strategy can be utilized in the future to accelerate our method.

IV. CONCLUSION

This paper has proposed the decay parameter adaptation framework for the nonlocal means method to remove Gaussian noise and speckle noise. The proposed method can adaptively determine the decay parameter for each image pixel by minimizing the pixel-wise MSE, which is estimated by approximating the unknown noise-free image and the noise with the global minimum MSE based denoised result and the corresponding method noise, respectively.

Quantitative comparisons based on the standard images show that the proposed method significantly outperforms some compared NLM methods by providing higher PSNR and SSIM values, and it performs better than the BM3D and DnCNN methods in most cases for removing Gaussian noise and speckle-noise. Furthermore, the proposed method has great potential applications to denoising real SAR, MR and US images due to its outstanding image detail preservation performance, which is very important in pattern recognition and medical diagnosis.

In general, the proposed method provides a universal framework for the parameter optimization in the NLM method. It can be easily extended to optimize such parameters as the search window and similarity window sizes. Meanwhile, the proposed method can be combined with existing patch-based denoising algorithms such as the PPB method and the OBNLM method to further improve their restoration performance. Our future work will be focused on the acceleration of the proposed method and its extension to remove Possion noise, Rician noise and impulse noise.

APPENDIX A

The derivation of the inequality $\frac{\partial var[v]}{\partial h} \neq 0$ is as follows.

The term $\frac{\partial var[v]}{\partial h}$ can be computed as:

$$\begin{aligned}\frac{\partial var[v]}{\partial h} &= 2 \cdot \frac{\partial(\mathbf{E}(v^2)) - (\mathbf{E}(v))^2}{\partial h} \\ &= 2 \cdot \left(\mathbf{E}\left(v \cdot \frac{\partial v}{\partial h}\right) - \mathbf{E}(v) \cdot E\left(\frac{\partial v}{\partial h}\right)\right) \\ &= 2 \cdot \left(\mathbf{E}\left(v \cdot \frac{\partial (I-u)}{\partial h}\right) - \mathbf{E}(v) \cdot \mathbf{E}\left(\frac{\partial (I-u)}{\partial h}\right)\right) \\ &= 2 \cdot \left(\mathbf{E}(v) \cdot \mathbf{E}\left(\frac{\partial u}{\partial h}\right) - \mathbf{E}\left(v \cdot \frac{\partial u}{\partial h}\right)\right) \\ &= -2 \cdot cov\left(v, \frac{\partial u}{\partial h}\right) \end{aligned} \tag{A.1}$$

For the convenience of computing $\frac{\partial u}{\partial h}$, we will consider its computation for any pixel at (x, y) in the image I. According to equation (1), $\frac{\partial u(x,y)}{\partial h}$ is computed as:

$$\begin{aligned}\frac{\partial u(x,y)}{\partial h} = &\frac{\sum\limits_{(p,q)\in\Omega} I(p,q)\frac{\partial \omega(x,y,p,q)}{\partial h}}{\sum\limits_{(p,q)\in\Omega} \omega(x,y,p,q)} \\ &- \frac{\sum\limits_{(p,q)\in\Omega} I(p,q)\omega(x,y,p,q) \sum\limits_{(p,q)\in\Omega} \frac{\partial \omega(x,y,p,q)}{\partial h}}{\left(\sum\limits_{(p,q)\in\Omega} \omega(x,y,p,q)\right)^2}\end{aligned} \tag{A.2}$$

where

$$\begin{aligned}\frac{\partial w(x,y,p,q)}{\partial h} &= 2 \cdot \exp\left(-\frac{||I(P(p,q)) - I(P(x,y))||^2_{2,a}}{h^2}\right) \\ &\quad \cdot \frac{||I(P(p,q)) - I(P(x,y))||^2_{2,a}}{h^3} \\ &= -2 \cdot \frac{w(x,y,p,q) ln(w(x,y,p,q))}{h}\end{aligned} \tag{A.3}$$

According to equations (A.2) and (A.3), $\frac{\partial u(x,y)}{\partial h}$ is expressed as:

$$\begin{aligned}&\frac{\partial u(x,y)}{\partial h} \\ &= \frac{\sum\limits_{(p,q)\in\Omega} (I(p,q) - u(x,y)) w(x,y,p,q) ln(w(x,y,p,q))}{-\frac{h}{2}\sum\limits_{(p,q)\in\Omega} \omega(x,y,p,q)}\end{aligned} \tag{A.4}$$

Because $0 < w(x,y,p,q) \leq 1$ and $ln(w(x,y,p,q)) \leq 0$, it follows that

$$\begin{aligned}&\sum_{(p,q)\in\Omega} I(p,q) w(x,y,p,q) ln(w(x,y,p,q)) \\ &\geq \sum_{(p,q)\in\Omega} I(p,q) w(x,y,p,q) \sum_{(p,q)\in\Omega} ln(w(x,y,p,q))\end{aligned} \tag{A.5}$$

According to the inequality (A.5), we have

$$\frac{\partial u(x,y)}{\partial h} \le \frac{2}{h}\left(\frac{\sum_{(p,q)\in\Omega} w(x,y,p,q)ln(w(x,y,p,q))}{\sum_{(p,q)\in\Omega}\omega(x,y,p,q)} - \sum_{(p,q)\in\Omega} ln(w(x,y,p,q))\right)u(x,y) \quad (A.6)$$

From the inequality (A.6), it can be seen that there will exist a constant $K(x,y)$ which will meet the following condition.

$$\frac{\partial u(x,y)}{\partial h} = K(x,y)u(x,y) \quad (A.7)$$

where

$$K(x,y) \le \frac{2}{h}\left(\frac{\sum_{(p,q)\in\Omega} w(x,y,p,q)ln(w(x,y,p,q))}{\sum_{(p,q)\in\Omega}\omega(x,y,p,q)} - \sum_{(p,q)\in\Omega} ln(w(x,y,p,q))\right) \quad (A.8)$$

According to equation (A.7), it is easy to derive that

$$\frac{\partial var[v]}{\partial h} = -2\cdot H\cdot cov(v,u) \quad (A.9)$$

where H is a two dimensional matrix of constants K expressed as:

$$H = \begin{pmatrix} K(1,1) & K(1,2) & \cdots & K(1,N) \\ K(2,1) & K(2,2) & \cdots & K(2,N) \\ \vdots & \vdots & \ddots & \vdots \\ K(M,1) & K(M,2) & \cdots & K(M,N) \end{pmatrix}, \quad (A.10)$$

where M and N denote the number of pixels in the horizontal and vertical dimensions of the image I, respectively.

For H, $H \neq 0$ holds because the noisy image I will not be completely homogeneous. Meanwhile, $cov(v,u) \neq 0$ because u and v are correlated. According to equation (A.9), it can be derived that $\frac{\partial var[v]}{\partial h} \neq 0$.

APPENDIX B

The two items $\frac{\partial \hat{bias}^2[u(x,y)]}{\partial h(x,y)}$ and $\frac{\partial \hat{var}[u(x,y)]}{\partial h(x,y)}$ are derived by computing the partial differential with respect to $h(x,y)$ on both sides of equation (14) and equation (15) as:

$$\frac{\partial \hat{bias}^2[u(x,y)]}{\partial h(x,y)} = \frac{\partial \hat{bias}^2[u(x,y)]}{\partial \hat{\omega}(x,y,p,q)}\cdot\frac{\partial \hat{\omega}(x,y,p,q)}{\partial h(x,y)} = 2\cdot\frac{\sum_{(p,q)\in\Omega}(\hat{s}(p,q)-\hat{s}(x,y))\hat{\omega}(x,y,p,q)}{\sum_{(p,q)\in\Omega}\hat{\omega}(x,y,p,q)} \cdot\left(\frac{\sum_{(p,q)\in\Omega}(\hat{s}(p,q)-\hat{s}(x,y))\frac{\partial \hat{w}(x,y,p,q)}{\partial h(x,y)}}{\sum_{(p,q)\in\Omega}\hat{\omega}(x,y,p,q)} - \frac{\sum_{(p,q)\in\Omega}(\hat{s}(p,q)-\hat{s}(x,y))\hat{\omega}(x,y,p,q)}{\left(\sum_{(p,q)\in\Omega}\hat{\omega}(x,y,p,q)\right)^2}\cdot\sum_{(p,q)\in\Omega}\frac{\partial \hat{w}(x,y,p,q)}{\partial h(x,y)}\right), \quad (A.11)$$

$$\frac{\partial \hat{var}[u(x,y)]}{\partial h(x,y)} = \frac{\partial \hat{var}[u(x,y)]}{\partial \hat{\omega}(x,y,p,q)}\cdot\frac{\partial \hat{\omega}(x,y,p,q)}{\partial h(x,y)} = 2\cdot\frac{\sum_{(p,q)\in\Omega}\hat{\eta}^*(p,q)\hat{\omega}(x,y,p,q)}{\sum_{(p,q)\in\Omega}\hat{\omega}(x,y,p,q)} \cdot\left(\frac{\sum_{(p,q)\in\Omega}\hat{\eta}^*(p,q)\frac{\partial \hat{w}(x,y,p,q)}{\partial h(x,y)}}{\sum_{(p,q)\in\Omega}\hat{\omega}(x,y,p,q)} - \frac{\sum_{(p,q)\in\Omega}\hat{\eta}^*(p,q)\hat{\omega}(x,y,p,q)}{\left(\sum_{(p,q)\in\Omega}\hat{\omega}(x,y,p,q)\right)^2}\cdot\sum_{(p,q)\in\Omega}\frac{\partial \hat{w}(x,y,p,q)}{\partial h(x,y)}\right), \quad (A.12)$$

where

$$\frac{\partial \hat{w}(x,y,p,q)}{\partial h(x,y)} = 2\cdot\exp\left(-\frac{||\hat{s}(P(p,q))-\hat{s}(P(x,y))||^2_{2,a}}{(h(x,y))^2}\right)\cdot\frac{||\hat{s}(P(p,q))-\hat{s}(P(x,y))||^2_{2,a}}{(h(x,y))^3} \quad (A.13)$$

ACKNOWLEDGMENT

The authors would like to thank the anonymous reviewers for their valuable suggestions and comments which improved the quality of this paper greatly. They would also like to thank Medical Ultrasound Laboratory at Huazhong University of Science and Technology for providing the liver ultrasound image.

REFERENCES

[1] Z. Gan, F. Zou, N. Zeng N, B. Xiong, and L. Liao, "Wavelet denoising algorithm based on NDOA compressed sensing for fluorescence image of microarray," *IEEE Access*, vol. 7, pp. 13338–13346, Jan. 2019.

[2] A. Kuijper, "Geometrical PDEs based on second-order derivatives of gauge coordinates in image processing," *Image Vis. Comput.*, vol. 27, no. 8, pp. 1023–1034, Jul. 2009.

[3] J. Zou, M. Shen, Y. Zhang, H. Li, G. Liu, and S. Ding, "Total variation denoising with non-convex regularizers," *IEEE Access*, vol. 7, pp. 4422–4431, 2018.

[4] W. Chen, Y. Shao, Y. Wang, Q. Zhang, Y. Liu, L. Yao, Y. Chen, G. Yang, and Z. Gui, "A novel total variation model for low-dose CT image denoising," *IEEE Access*, vol. 6, pp. 78892–78903, 2018.

[5] A. Buades, B. Coll, and J.-M. Morel, "A non-local algorithm for image denoising," in *Proc. IEEE Comput. Soc. Conf. Comput. Vis. Pattern Recognit.*, San Diego, CA, USA, Jun. 2005, pp. 60–65.

[6] K. Zhang, W. Zuo, Y. Chen, D. Meng, and L. Zhang, "Beyond a Gaussian denoiser: Residual learning of deep CNN for image denoising," *IEEE Trans. Image Process.*, vol. 26, no. 7, pp. 3142–3155, Jul. 2017.

[7] J. Boulanger, C. Kervrann, and P. Bouthemy, "Space-time adaptation for patch-based image sequence restoration," *IEEE Trans. Pattern Anal. Mach. Intell.*, vol. 29, no. 6, pp. 1096–1102, Jun. 2007.

[8] C. Kervrann and J. Boulanger, "Local adaptivity to variable smoothness for exemplar-based image regularization and representation," *Int. J. Comput. Vis.*, vol. 79, no. 1, pp. 45–69, Aug. 2008.
[9] X. Li, H. He, R. Wang, and J. Cheng, "Superpixel-guided nonlocal means for image denoising and super-resolution," *Signal Process.*, vol. 124, no. 2, pp. 173–183, 2016.
[10] C. A. Deledalle, V. Duval, and J. Salmon, "Non-local methods with shape-adaptive patches (NLM-SAP)," *J. Math. Imag. Vis.*, vol. 43, no. 2, pp. 103–120, Jun. 2012.
[11] T. Brox, O. Kleinschmidt, and D. Cremers, "Efficient nonlocal means for denoising of textural patterns," *IEEE Trans. Image Process.*, vol. 17., no. 7, pp. 1083–1092, Jul. 2008.
[12] K. Dabov, A. Foi, V. Katkovnik, and K. Egiazarian, "Image denoising by sparse 3-D transform-domain collaborative filtering," *IEEE Trans. Image Process.*, vol. 16, no. 8, pp. 2080–2095, Aug. 2007.
[13] T. Tasdizen, "Principal neighborhood dictionaries for nonlocal means image denoising," *IEEE Trans. Image Process.*, vol. 18, no. 12, pp. 2649–2660, Dec. 2009.
[14] A. Kumar, "Nonlocal means image denoising using orthogonal moments," *Appl. Opt.*, vol. 54, no. 27, pp. 8156–8165, Sep. 2015.
[15] C.-A. Deledalle, L. Denis, and F. Tupin, "Iterative weighted maximum likelihood denoising with probabilistic patch-based weights," *IEEE Trans. Image Process.*, vol. 18, no. 12, pp. 2661–2672, Dec. 2009.
[16] C.-A. Deledalle, L. Denis, G. Poggi, F. Tupin, and L. Verdoliva, "Exploiting patch similarity for SAR image processing: The nonlocal paradigm," *IEEE Signal Process. Mag.*, vol. 31, no. 4, pp. 69–78, Jul. 2014.
[17] P. Coupé, P. Hellier, C. Kervrann, and C. Barillot, "Nonlocal means-based speckle filtering for ultrasound images," *IEEE Trans. Image Process.*, vol. 18, no. 10, pp. 2221–2229, Oct. 2009.
[18] Y. Zhou, H. Zang, S. Xu, H. He, J. Lu, and H. Fang, "An iterative speckle filtering algorithm for ultrasound images based on Bayesian non-local means filter model," *Biomed. Signal Process. Control*, vol. 48, pp. 104–117, Feb. 2019.
[19] C. Zuo, L. Jovanov, B. Goossens, H. Q. Luong, W. Philips, Y. Liu, and M. Zhang, "Image denoising using quadtree-based nonlocal means with locally adaptive principal component analysis," *IEEE Signal Process. Lett.*, vol. 23, no. 4, pp. 434–438, Apr. 2016.
[20] L. H. Breivik, S. R. Snare, E. N. Steen, and A. H. Solberg, "Real-time nonlocal means based despeckling," *IEEE Trans. Ultrason., Ferroelectr., Freq. Control*, vol. 64, no. 6, pp. 959–977, Jun. 2017.
[21] G. Liu and H. Zhong, "Nonlocal means filter for polarimetric SAR data despeckling based on discriminative similarity measure," *IEEE Geosci. Remote Sens. Lett.*, vol. 11, no. 2, pp. 514–518, Feb. 2014.
[22] Y. Zhan, M. Ding, L. Wu, and X. Zhang, "Nonlocal means method using weight refining for despeckling of ultrasound images," *Signal Process.*, vol. 103, pp. 201–213, Oct. 2014.
[23] L. Torres, S. J. Sant'Anna, C. da Costa Freitas, and A. C. Frery, "Speckle reduction in polarimetric SAR imagery with stochastic distances and nonlocal means," *Pattern Recognit.*, vol. 47, no. 1, pp. 141–157, Jan. 2014.
[24] P. Shen, C. Wang, H. Gao, and J. Zhu, "An adaptive nonlocal mean filter for PolSAR data with shape-adaptive patches matching," *Sensors*, vol. 18, no. 7, p. 2215, Jul. 2018.
[25] H. Zhong, Y. Li, and L. Jiao, "SAR image despeckling using Bayesian nonlocal means filter with sigma preselection," *IEEE Geosci. Remote Sens. Lett.*, vol. 8, no. 4, pp. 809–813, Jul. 2011.
[26] C. Jojy, M. S. Nair, G. R. K. S. Subrahmanyam, and R. Riji, "Discontinuity adaptive non-local means with importance sampling unscented Kalman filter for de-speckling SAR images," *IEEE J. Sel. Topics Appl. Earth Observ. Remote Sens.*, vol. 6, no. 4, pp. 1964–1970, Aug. 2013.
[27] H. Zhong, J. Zhang, and G. Liu, "Robust polarimetric SAR despeckling based on nonlocal means and distributed Lee filter," *IEEE Trans. Geosci. Remote Sens.*, vol. 52, no. 7, pp. 4198–4280, Jul. 2014.
[28] J. Yang, J. Fan, D. Ai, X. Wang, Y. Zheng, S. Tang, and Y. Wang, "Local statistics and non-local mean filter for speckle noise reduction in medical ultrasound image," *Neurocomputing*, vol. 195, pp. 88–95, Jun. 2016.
[29] W. Ni and X. Gao, "Despeckling of SAR image using generalized guided filter with Bayesian nonlocal means," *IEEE Trans. Geosci. Remote Sens.*, vol. 54, no. 1, pp. 567–579, Jan. 2016.
[30] C. Sutour, C.-A. Deledalle, and J.-F. Aujol, "Adaptive regularization of the NL-means: Application to image and video denoising," *IEEE Trans. Image Process.*, vol. 23, no. 8, pp. 3506–3521, Aug. 2014.
[31] S. Parrilli, M. Poderico, C. V. Angelino, and L. Verdoliva, "A nonlocal SAR image denoising algorithm based on LLMMSE wavelet shrinkage," *IEEE Trans. Geosci. Remote Sens.*, vol. 50, no. 2, pp. 606–616, Feb. 2012.
[32] J. Joseph, J. Sivaraman, R. Periyasamy, and V. R. Simi, "Noise based computation of decay control parameter in nonlocal means filter for MRI restoration," *J. Med. Imag. Health Inform.*, vol. 6, no. 4, pp. 1027–1037, Aug. 2016.
[33] P. Coupé, P. Yger, S. Prima, P. Hellier, C. Kervrann, and C. Barillot, "An optimized blockwise nonlocal means denoising filter for 3-D magnetic resonance images," *IEEE Trans. Med. Imag.*, vol. 27, no. 4, pp. 425–441, Apr. 2008.
[34] D. Van De Ville and M. Kocher, "SURE-based non-local means," *IEEE Signal Process. Lett.*, vol. 16, no. 11, pp. 973–976, Nov. 2009.
[35] V. Duval, J.-F. Aujol, and Y. Gousseau, "A bias-variance approach for the nonlocal means," *SIAM J. Imag. Sci.*, vol. 4, no. 2, pp. 760–788, Jun. 2011.
[36] V. Doré and M. Cheriet, "Robust NL-means filter with optimal pixel-wise smoothing parameter for statistical image denoising," *IEEE Trans. Signal Process.*, vol. 57, no. 5, pp. 1703–1716, May 2009.
[37] X. Hao, S. Gao, and X. Gao, "A novel multiscale nonlinear thresholding method for ultrasonic speckle suppressing," *IEEE Trans. Med. Imag.*, vol. 18, no. 9, pp. 787–794, Sep. 1999.
[38] T. Loupas, W. N. McDicken, and P. L. Allan, "An adaptive weighted median filter for speckle suppression in medical ultrasonic images," *IEEE Trans. Circuits Syst.*, vol. 36, no. 1, pp. 129–135, Jan. 1989.
[39] A. Achim, A. Bezerianos, and P. Tsakalides, "Novel Bayesian multiscale method for speckle removal in medical ultrasound images," *IEEE Trans. Med. Imag.*, vol. 20, no. 8, pp. 772–783, Aug. 2001.
[40] F. Argenti and G. Torricelli, "Speckle suppression in ultrasonic images based on undecimated wavelets," *EURASIP J. Appl. Signal Process.*, vol. 2003, Dec. 2003, Art. no. 379638.
[41] F. Argenti, T. Bianchi, and L. Alparone, "Multiresolution MAP despeckling of SAR images based on locally adaptive generalized Gaussian pdf modeling," *IEEE Trans. Image Process.*, vol. 15, no. 11, pp. 3385–3399, Nov. 2006.
[42] E. Cuevas, L. Enríquez, D. Zaldívar, and M. Pérez-Cisneros, "A selection method for evolutionary algorithms based on the golden section," *Expert Syst. Appl.*, vol. 106, pp. 183–196, Sep. 2018.
[43] G. Gilboa, N. Sochen, and Y. Y. Zeevi, "Estimation of optimal PDE-based denoising in the SNR sense," *IEEE Trans. Image Process.*, vol. 15, no. 8, pp. 2269–2280, Aug. 2006.
[44] J. Darbon, A. Cunha, T. F. Chan, G. J. Jensen, and S. Osher, "Fast nonlocal filtering applied to electron cryomicroscopy," in *Proc. 5th IEEE Int. Symp. Biomed. Imag.*, Paris, France, May 2008, pp. 1331–1334.
[45] S. M. Smith and J. M. Brady, "SUSAN—A new approach to low level image processing," *Int. J. Comput. Vis.*, vol. 23, no. 1, pp. 45–78, May 1997.
[46] Y. Romano and M. Elad, "Boosting of image denoising algorithms," *SIAM J. Imag. Sci.*, vol. 8, no. 2, pp. 1187–1219, 2015.
[47] *Training Images*. Accessed: Jul. 1, 2019. [Online]. Available: https://github.com/cszn/DnCNN/tree/master/TrainingCodes/DnCNN_TrainingCodes_v1.0/data/Train400
[48] Z. Wang, A. C. Bovik, H. R. Sheikh, and E. P. Simoncelli, "Image quality assessment: From error visibility to structural similarity," *IEEE Trans. Image Process.*, vol. 13, no. 4, pp. 600–612, Apr. 2004.
[49] *The SSIM Index for Image Quality Assessment*. Accessed: Jul. 1, 2019. [Online]. Available: https://www.ece.uwaterloo.ca/~z70wang/research/ssim/
[50] L. He and I. R. Greenshields, "A nonlocal maximum likelihood estimation method for Rician noise reduction in MR images," *IEEE Trans. Med. Imag.*, vol. 28, no. 2, pp. 165–172, Feb. 2009.
[51] *MRI Image*. Accessed: Jul. 1, 2019. [Online]. Available: http://www.ohsu.edu/xd/research/centers-institutes/airc/airc-7t-instrument.cfm
[52] *SAR Image*. Accessed: Jul. 1, 2014. [Online]. Available: http://www.sandia.gov/RADAR/sar.html
[53] V. Behar, D. Adam, and Z. Friedman, "A new method of spatial compounding imaging," *Ultrasonics*, vol. 41, no. 5, pp. 377–384, Jul. 2003.

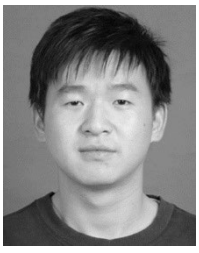

YI ZHAN received the B.S. degree from the South China University of Technology and the Ph.D. degree in biomedical engineering from the Huazhong University of Science and Technology, Wuhan, China, in 2014. His research interests include medical image denoising, image segmentation, and image registration.

JINBO WU received the B.S. degree in mechanical manufacture and automation from the Wuhan University of Technology, China, in 1996, and the M.S. and Ph.D. degrees in mechanical electronic engineering from the Huazhong University of Science and Technology (HUST), Wuhan, China, in 2002 and 2007, respectively, where he is currently an Associate Professor with the School of Naval Architecture and Ocean Engineering. His research interests include image processing, control of nonlinear systems, and robotics.

MINGYUE DING received the B.S. degree from the Beijing University of Aeronautics and Astronautics, Beijing, China, in 1982, the M.S. degree from the Chinese University of Electronics Science and Technology, Sichuan, China, in 1985, and the Ph.D. degree from the Huazhong University of Science and Technology, Wuhan, China, in 1988, where he is currently a Professor with the Department of Biomedical Engineering, School of Life Science and Technology. His research interests include medical image analysis, ultrasound imaging, and image-guided surgery and therapy.

XUMING ZHANG received the B.S. and M.S. degrees in material science and engineering from the Wuhan University of Technology, China, in 1998 and 2001, respectively, and the Ph.D. degree from Shanghai Jiaotong University, China, in 2005. From 2006 to 2008, he worked in the field of mechanical and electrical engineering at the Huazhong University of Science and Technology (HUST) as a Postdoctoral Researcher. From 2008 to 2009, he pursued his Postdoctoral Research with the University of California at Davis, USA. Since 2009, he has been an Associate Professor with the Department of Biomedical Engineering, HUST. His research interests include image de-noising and image registration.